The Astrophysical Journal Letters, 940:L51 (10pp), 2022 December 1 https://doi.org/10.3847/2041-8213/ac98c5

A New Era of Intracluster Light Studies with JWST

Mireia Montes[1,2] and Ignacio Trujillo[1,2]
[1] Instituto de Astrofísica de Canarias, c/ Vía Láctea s/n, E-38205 La Laguna, Tenerife, Spain; mireia.montes.quiles@gmail.com
[2] Departamento de Astrofísica, Universidad de La Laguna, E-38205 La Laguna, Tenerife, Spain
Received 2022 August 31; revised 2022 October 6; accepted 2022 October 8; published 2022 December 1

Abstract

Still largely unexplored, the diffuse light in clusters of galaxies traces the past and ongoing buildup of these massive structures. Here we present the first comprehensive study of the intracluster light (ICL) of the cluster SMACS J0723.3–7327 ($z = 0.39$) using the JWST Early Release Observations. These deep and high spatial resolution images allow the study of the ICL with a high signal-to-noise ratio up to a radial distance of ∼400 kpc, twice as far with respect to previous HST studies of intermediate-redshift clusters. This opens up the possibility of exploring the rich mixture of processes that are building the ICL. We find that the inner parts of this cluster ($R < 100$ kpc) are built through a major merger, while the outer parts ($R > 100$ kpc) are mainly produced by the tidal stripping of Milky Way–like satellites. We also find that the slope of the stellar mass density radial profile of the ICL of this cluster ($\alpha_{3D} = -2.47 \pm 0.13$) closely follows the predicted dark matter halo slope ($\alpha_{3D,DM} = -2.6$ to -2), supporting the idea that both components have a similar shape and thus the potential of using the ICL as a tracer of the dark matter distribution in clusters of galaxies. Future JWST studies of the ICL are set to revolutionize our understanding of cluster formation and will be crucial to improve the gravitational lensing mass maps of these structures and thus accurately characterize the properties of the first galaxies.

Unified Astronomy Thesaurus concepts: James Webb Space Telescope (2291); Galaxy clusters (584); Dark matter distribution (356)

1. Introduction

During the past 20 yr, observations have shown that the intracluster light (ICL) is a ubiquitous feature in galaxy clusters (Feldmeier et al. 2002; Krick & Bernstein 2007; Kluge et al. 2020). During encounters between galaxies in groups and clusters, stars are freed from their hosts and end up populating the space between the galaxies. After some time, these unbound stars form the characteristic diffuse glow of the ICL. Consequently, this light is a signature of the assembly of clusters of galaxies (see Montes 2019; Contini 2021; Montes 2022, for recent reviews).

The ICL has been shown to be an unexpected tool to study groups and clusters of galaxies in detail, allowing us to infer not only their assembly history but also their radius and even dark matter distribution (Montes & Trujillo 2019; Alonso Asensio et al. 2020; Deason et al. 2021; Gonzalez et al. 2021). For example, Mahler et al. (2022) showed that the inclusion of the ICL as a prior to model the mass distribution of the cluster SMACS J0723.3–7327 resulted in more accurate mass maps (1.″08 of rms compared to 1.″26 of rms without ICL). These results show the extraordinary potential of using the ICL as an accurate dark matter tracer.

Observations of the ICL of intermediate-redshift clusters have been, for the most part, limited to the blue part of the spectrum. These observations show clear radial gradients in colors indicating radial gradients in metallicity (e.g., Iodice et al. 2017; Mihos et al. 2017; DeMaio et al. 2018; Montes et al. 2021) and, in some cases, age (e.g., Montes & Trujillo 2014; Morishita et al. 2017; Montes & Trujillo 2018). Consequently, exploring the ICL distribution and mass fraction of intermediate-redshift clusters using only blue filters is prone to artificial biases. In this context, it is clear that deep infrared (IR) imaging with high spatial resolution, as provided by JWST (Rigby et al. 2022), would be a major step forward in the study of clusters. First, the inclusion of IR wavelengths in the study of the stellar populations would constrain their properties (age and metallicity) better than using optical data alone (e.g., Worthey 1994). Second, the IR explores the rest-frame optical/near-IR wavelengths of more distant systems, enabling a better characterization of the stellar mass distribution of these objects.

The advent of JWST marks a new era in the detection and study of the low surface brightness universe. The exceptional IR sensitivity of JWST's detectors holds great promise for the detection of extremely low surface brightness features. The aim of this work is to showcase, for the first time, the potential of JWST observations to study the diffuse light in clusters of galaxies.

Throughout this work, we adopt a standard cosmological model with the following parameters: $H_0 = 70\ \mathrm{km\ s^{-1}\ Mpc^{-1}}$, $\Omega_m = 0.3$, and $\Omega_\Lambda = 0.7$. The redshift of this cluster is $z = 0.39$, corresponding to a spatial scale of $5.3\ \mathrm{kpc\ arcsec^{-1}}$. All magnitudes in this paper are in the AB magnitude system.

2. Data

The JWST Near Infrared Camera (NIRCam[3]; Rieke et al. 2005) imaging is obtained at 0.62.3 μm (0.″031/pixel, short-wavelength channel) and 2.4–5.0 μm (0.″063/pixel, long-wavelength channel) simultaneously over a 9.7 arcmin^2 field of view. NIRCam uses a dichroic to observe in both channels in roughly the same field of view. The camera consists of two modules (A and B) separated by an ∼44″ gap. Each of the detectors contains 2048×2048 pixels. Only the inner

[3] https://jwst-docs.stsci.edu/jwst-near-infrared-camera/nircam-instrumentation/nircam-detector-overview

2040×2040 pixels are for science, and the outer 4 pixel wide border consists of reference pixels used for calibration. The short-wavelength channel has four detectors and therefore twice the resolution, and the long-wavelength channel has one in each of the modules.

Deep observations of the cluster SMACS J0723.3–7327 (hereafter SMACS 0723; Repp & Ebeling 2018) were taken with the NIRCam filters F090W, F150W, F200W, F277W, F356W, and F444W. NIRCam module B was centered on the cluster and module A on an adjacent field. The cluster was observed on 2022 June 7 with several instruments on board JWST as part of the observatory's Early Release Observations (ERO; Pontoppidan et al. 2022). The primary data set used for this work is based on the images obtained with NIRCam, retrieved from the Mikulski Archive for Space Telescopes (MAST).[4]

2.1. Reprocessing of the Calibrated Files

The calibrated, coadded final (stage 3) released images present light gradients across the image, making them unsuitable to study the ICL of this cluster.

In this section, we will explain our attempt at improving the data quality, rereducing these images in a more suitable way for the purposes of this paper. In this work, we concentrate our efforts on the long-wavelength channel. The short-wavelength channel needs a more elaborate rereduction that is beyond the scope of this work. See Appendix B for more details.

2.1.1. Long-wavelength Channel

The long-wavelength channel consists of two detectors, one for each module. The pixel scale of this channel is 0.063″ /pixel The recalibration of the long-wavelength channel images was done in a two-step process. The light gradients in the final calibrated images (stage 3) are clearly an artifact. They are different from the ones observed in the short-wavelength filters and not present in the RELICS Hubble Space Telescope images (Coe et al. 2019). The origin of these light gradients is not clear, but they are observed in both the individual frames and the final coadd of all of the long-wavelength images.

To correct these gradients, first, we downloaded the calibrated (stage 2) individual frames of the F277W, F356W, and F444W bands from MAST. For the first step of the process, in each of the frames, we masked all galaxies, foreground and background objects, and the central parts of the cluster. Then, we fitted a second-degree 2D polynomial (a plane) to the masked frame to model the gradient seen in the individual frames. The size of this plane is larger than the physical extent of the ICL in the images. This ensures that we are only correcting the gradient in the image while preserving the diffuse light of the cluster. In Appendix A, we show an example of this process.

With the background of the individual images corrected, we created a preliminary coadd of the nine exposure frames per filter. This first coadd is then used to build a more accurate mask of the cluster, adding manually masked regions to cover the central parts of the image and minimize ICL contamination. This improved mask is then applied to the individual frames to obtain a more reliable model of the light gradient for each of the frames. Once the frames are corrected from this gradient, we use SWarp (Bertin 2010) to create the final coadd. The background of the final images shows negative values caused by a slight overcorrection during the gradient correction process. Therefore, we computed and subtracted a constant background value from the final coadded images. The values of this background are -0.0011 (0.36σ), -0.0007 (0.25σ), and -0.0011 (0.32σ) MJy sr^{-1} for F277W, F356W, and F444W, respectively.

Note that we have used the original released images (Pontoppidan et al. 2022). It is known that there is a systematic magnitude offset due to the 20% higher throughput of the filters in the long-wavelength channel (Rigby et al. 2022). Therefore, we correct the photometry of the images using the offsets listed in Adams et al. (2022). The offsets are $+0.223$, $+0.163$, and $+0.162$ for the F277W, F356W, and F444W bands, respectively. The zero-points to convert to mag arcsec^{-2} of each image are computed using the transformation in Appendix C.

The rereduced images of the long-wavelength channels are available.[5] Although we do not make use of them in this work, we have also made available the rereduced images of the short-wavelength channel.

2.2. Masking

The study of the ICL in clusters of galaxies requires very careful masking of sources to reduce contamination that can affect the intrinsic properties of this light. In the case of deep images, this masking must be optimized for faint and small objects and bright and large objects, background, and foreground, as well as belonging to the cluster. We use `SExtractor`'s segmentation map (Bertin & Arnouts 1996) to build the masks for these images.

As a single setup for the detection and masking of both types of sources is unfeasible, we used a similar approach as in Montes & Trujillo (2018) and Montes et al. (2021): two `SExtractor` runs, one to detect small sources ("hot" mode) and another to detect larger, more extended objects ("cold" mode). We use this approach on a median F277W + F356W + F444W image. In the case of the "hot" mode, we unsharp-masked the original image to enhance the contrast of the smallest sources, particularly in the central parts of the cluster. To make the unsharp-masked image, we convolved the original image with a median box filter with a side of 5 pixels, and then we subtracted it from the original. This "hot" mask was further expanded by 4 pixels. The faintest sources we mask are $\sim$26.5 mag in F277W. The brightest cluster galaxy (BCG) is left unmasked in both the "hot" and "cold" masks.

The final mask was again visually inspected to manually mask any remaining light that was missed by the process described above. We typically mask extended sources down to 26 mag arcsec^{-2} in F277W. The spikes of the bright stars were also manually masked. In this final mask, all of the objects are masked except for the BCG and ICL.

2.3. Surface Brightness Limits

Our goal is to study the low surface brightness features in SMACS 0723 down to the faintest surface brightness possible. For this reason, we need to know how deep our images are by

[4] https://outerspace.stsci.edu/display/MASTDATA/JWST+AWS+Bulk+Download+Scripts

[5] https://www.dropbox.com/sh/zzb7fl1j0vl1vit/AABW1uz06Vn2XGCYAmOJIbega?dl=0

estimating the surface brightness limits that they reach. To obtain these limits, we calculate the rms per pixel of the final masked images and apply the formula given in Román et al. (2020) to transform it to the typical $10'' \times 10''$ size. The 3σ surface brightness limits for the long-wavelength channel are listed in Table 1.

While the above limiting surface brightnesses are representative of the local depth, the current global background of the data is still affected by mild gradients left during the rereduction process. Therefore, we conservatively decided not to explore the surface brightness profiles of the ICL beyond $\mu_{\rm F444W} \sim 28$ mag arcsec^{-2}. In Figure 2, the surface brightness profiles are shown down to $\mu_{\rm F444W} \sim 28$ mag arcsec^{-2} ($\sim$350 kpc).

Table 1
Summary of the NIRCam Observations Used in This Work

Filter	Channel	Exp. Time (s)	Surface Brightness Limits[a] (mag arcsec^2)
F277W	Long	7537.2	31.28
F356W	Long	7537.2	31.32
F444W	Long	7537.2	31.10

Note.
[a] The surface brightness limits correspond to a sky fluctuation of 3σ in an area of 10×10 arcsec^2.

3. The ICL of SMACS 0723

Object SMACS 0723 is a cluster at z = 0.39 discovered as part of the southern extension of the Massive Cluster Survey (Repp & Ebeling 2018) with a mass of $M_h = 8.39^{+0.33}_{-0.34} \times 10^{14} M_\odot$ (Coe et al. 2019). This cluster was selected for the JWST's ERO for its gravitational lensing potential, as shown by the prominent lensed arcs and high latitude (i.e., low zodiacal emission; Pontoppidan et al. 2022).

Figure 1 shows the final rereduced images of SMACS 0723. The top panel is an RGB color-composite image of the F277W, F356W, and F444W filters with an average of these three filters as a black-and-white background. The most notable features in the image are highlighted: two east streams (1 and 2), the giant west loop, and plumes east and west of the BCG. East stream 1 is located 150 kpc from the BCG, while east stream 2 is at 243 kpc. The giant west loop covers a diameter of 100 kpc, from 150 to 250 kpc from the center of the BCG. The width of the loop is quite homogeneous throughout the structure ($\sim$30 kpc). This suggests that it could be the remains of the tidal destruction of a galaxy of similar diameter. This will be discussed in the next sections.

The plumes seen in the center of the cluster span between 25 and 100 kpc from the BCG. They seem to be the result of the interaction of the BCG with a massive galaxy (a mechanism suggested in, e.g., Lauer 1988). The inset in the top panel of Figure 1 shows a zoom-in into the central part of the cluster to show the plumes more clearly.

The bottom panel of Figure 1 shows the image average of the three filters with two isocontours: one representative of the galaxies of the cluster (red; 25 mag arcsec^{-2}) and one representative of the ICL at a distance of $\sim$350 kpc from the center of the BCG (orange; 27.5 mag arcsec^{-2}).

3.1. Radial Surface Brightness Profiles of the BCG + ICL

In this section, we show the surface brightness radial profiles along the two semimajor axes of the cluster. This is done to highlight the asymmetries that are concentrated along this axis. We followed a similar approach as in Montes et al. (2021).

We masked everything except for a 20° wide section toward the east and a 20° wide section toward the west. All of the objects, except the BCG and the ICL, are also masked within these regions. We derived the radial profiles in each of the three bands in 51 circular logarithmic-spaced bins from 0″ to 72″(or 380 kpc). The profiles for the east (right panel) and west (left panel) directions are shown in Figure 2. The insets in Figure 2 show the region used to derive the profiles. The errors, smaller than the size of the markers, are computed as the quadratic sum of the rms scatter of the signal and the rms scatter of the background for each bin. The profiles are corrected for the extinction of the galaxy ($E(B-V) = 0.193$; Schlafly & Finkbeiner 2011) using the Cardelli et al. (1989) extinction law. The gaps in the profiles correspond to masked regions in the images.

3.2. Color and Stellar Mass Density Profiles

The left panel of Figure 3 shows the F277W–F444W color profiles for the east (orange squares) and west (pink circles) profiles down to 300 kpc from the center of the BCG. The errors in the color profiles are the combination of the errors from the surface brightness radial profiles. As the outer parts of the images are more prone to systematics on the background subtraction, we conservatively show the radial color profiles down to a radial distance of $\sim$300 kpc.

In the color profile plot, we also indicate the position of the features highlighted in Figure 1. For instance, the position of the giant west loop is evidenced by the colors becoming bluer from 150 to 250 kpc in the west profile. Instead, the east streams appear as bumps in the east color profiles, indicating that the ICL is being enriched by the addition of metal-rich stars. The plumes at each side of the BCG coincide with the almost constant color profile in the inner $\sim$100 kpc in both the east and west color profiles, a signature of a major merger, as the merger will lead to the flattening of the metallicity gradient of the BCG (e.g., White 1980).

The right panel of Figure 3 shows the stellar mass density profiles of SMACS 0723 for the east (orange) and west (pink) profiles. A rest-frame 3.6 μm filter would be the most representative tracer of the underlying stellar mass distribution (e.g., Sheth et al. 2010). Therefore, we used the F444W band as a reference, as it is the closest to a 3.6 μm filter at the redshift of SMACS 0723. To estimate the surface stellar mass density profile, we apply Equation (1) in Montes & Trujillo (2014) to transform the F444W surface brightness profile to stellar mass density. We used the mass-to-light ratio (M/L) predictions in the Spitzer IRAC 3.6 μm band from the E-MILES models (Vazdekis et al. 2016).

The BCG+ICL profiles of clusters at intermediate redshifts have negative gradients of both metallicity and age (e.g., Montes & Trujillo 2014; Morishita et al. 2017; Montes & Trujillo 2018). Lacking precise information about the age and metallicity of the BCG and ICL of this cluster, we took two M/L ratios, for age 7 Gyr and [M/H] = 0.22 (0.70; solid lines) and age 1.5 Gyr and [M/H] = −0.7 (0.18; dashed lines), based on the values of age and metallicity of the

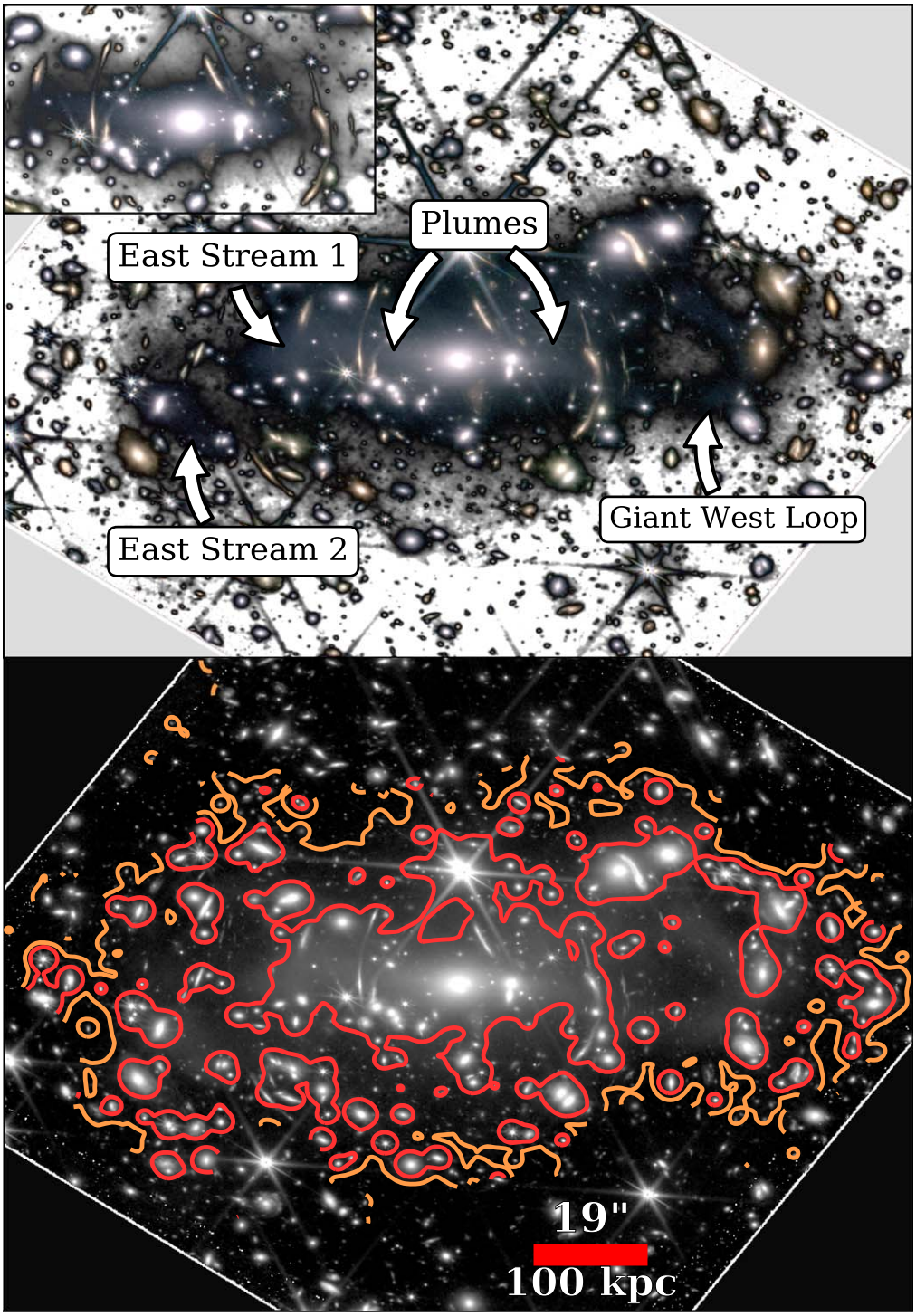

Figure 1. Cluster SMACS 0723. The top panel shows an RGB composite of the long-wavelength bands with a black-and-white background that is an average of the three filters. Some of the most prominent features in the ICL of the cluster are marked with arrows. The inset in the top panel is to better show the features in the center of the cluster. The bottom panel shows an average of the three long-wavelength bands with two isocontours overplotted: 25 (red) and 27.5 (orange) mag arcsec^2. North is up, and east is left.

Frontier Fields clusters for the center and ICL from Montes & Trujillo (2018). By selecting these two extreme predictions for the M/L, we ensure that the most likely stellar mass density profile of the cluster is within the two lines in the right panel of Figure 3.

Both stellar mass density profiles, east and west, roughly follow a power-law profile. The profiles also present the different features highlighted in Figure 1, like the giant west loop dip at ∼200 kpc and the bumps of east streams 1 (150 kpc) and 2 (240 kpc).

4. Discussion and Conclusions

The results presented in this work show the extraordinary potential of JWST to unravel the physical mechanisms behind the origin and evolution of the ICL. However, the current JWST NIRCAM data reduction is not yet low surface

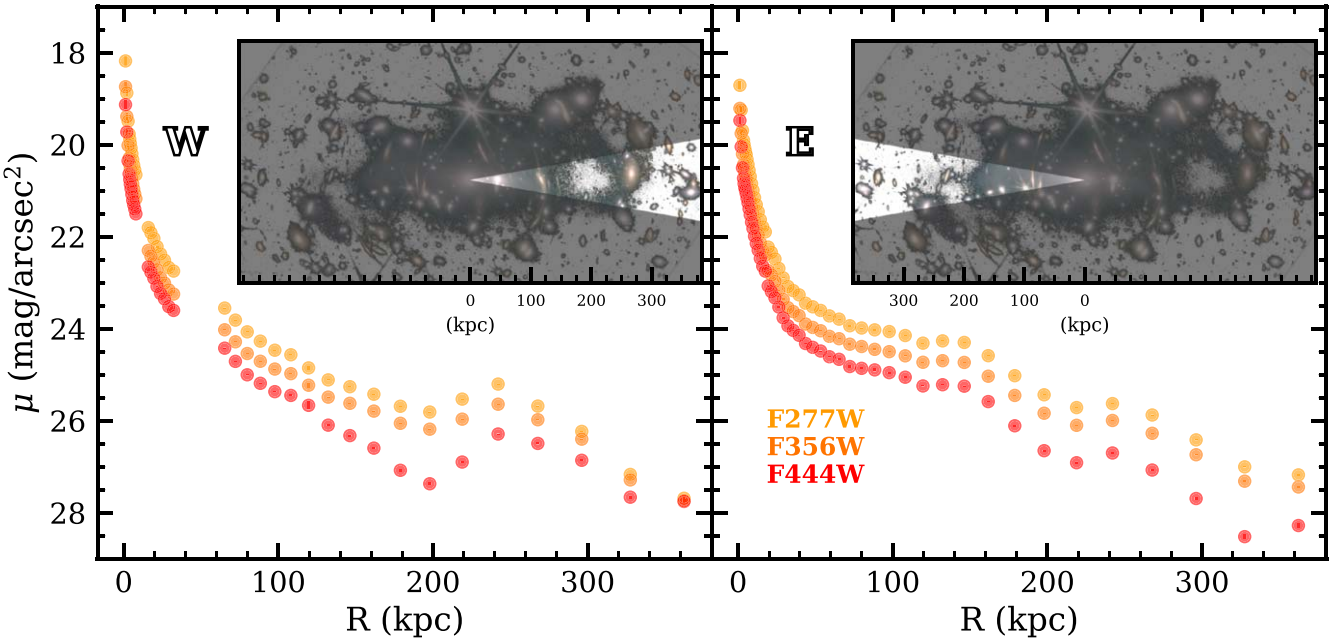

Figure 2. Surface brightness profiles as a function of radius for the BCG + ICL of SMACS 0723 for the F277W (yellow), F356W (orange), and F444W (red) bands. The left panel shows the profiles toward the west, while the right panel shows the profiles toward the east. The insets in both panels indicate the regions where the profiles were extracted.

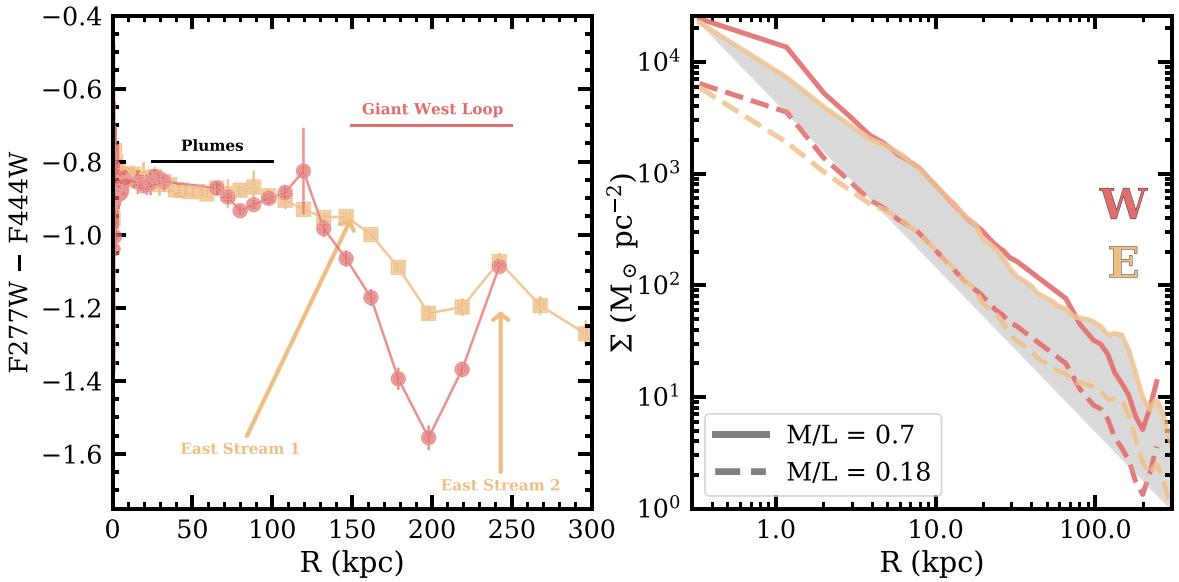

Figure 3. Left panel: F277W−F444W radial color profile of the BCG+ICL of SMACS 0723. The features seen in the ICL are highlighted in the plot. The east color profile is in orange (squares), while the west profile is in pink (circles). Right panel: stellar mass density radial profile of the BCG+ICL of SMACS 0723. The solid line indicates the density profile derived using an M/L of 0.7, and the dashed line has an M/L of 0.18. The gray shaded area indicates the range of all possible stellar mass density profiles assuming an M/L ranging from 0.7 to 0.18. For illustrative purposes, this is applied in this figure for the east profile. The center of the profile is assumed to have an M/L of 0.7. Note that the *X*-axis in the right panel is in logarithmic scale.

brightness–friendly. A tailored data reduction is a must in order to take the most advantage of the observations to study the faintest surface brightness features.

4.1. ICL Formation in SMACS 0723

The asymmetry of the diffuse light in SMACS 0723, along the east–west direction, means that the ICL of this cluster is still forming. The signature of this formation process can be seen in the prominent features that show up in both the surface brightness radial profiles in Figure 2 and the radial color profile in the left panel of Figure 3. In the following, we will discuss these features in detail.

4.1.1. The Giant West Loop and the East Streams

Early observations showed that the ICL originates from the tidal stripping of satellite galaxies as they interact inside the cluster (e.g., Gregg & West 1998; Mihos et al. 2005). This appears to be the origin of the features observed at larger radii, such as the east streams and the giant west loop in Figure 4.

The circular shape of the giant west loop is composed of two parts. Its left side corresponds to the diffuse light from the

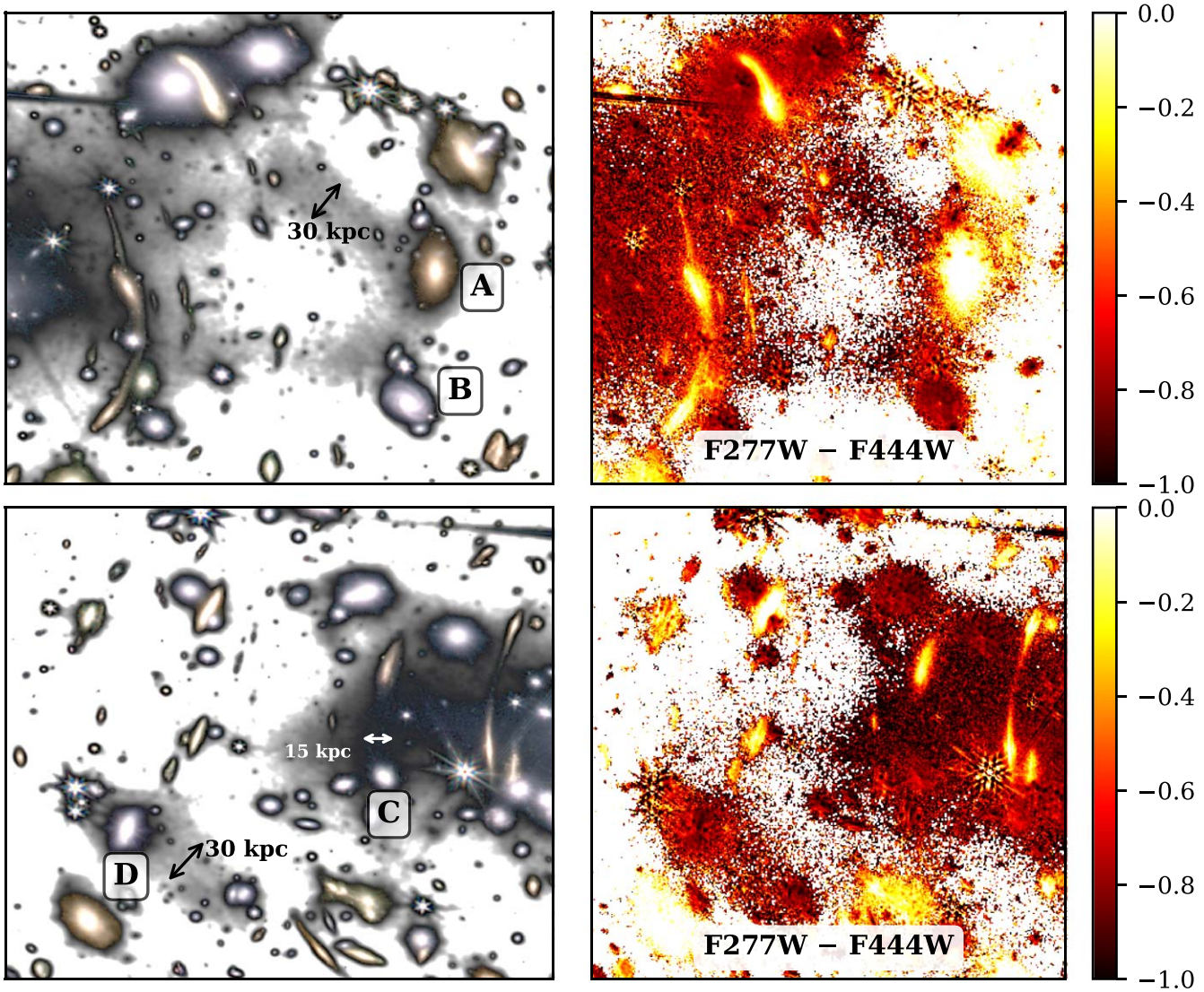

Figure 4. Zoom-ins to the different tidal features of SMACS 0723. The left panels show the RGB composite images, while the right panels show the F277W−F444W color maps. The upper panels show the giant west loop, and the lower panels show the east streams. The width of the different features is indicated with arrows.

center of the cluster rapidly decreasing. The right arc-like shape is likely the debris of a single stellar stream. The constant width of this feature (∼30 kpc) and homogeneous color is consistent with being a single stellar stream. In Figure 4 (upper left panel), we show the RGB color-composite image of the region, labeling two of the galaxies that could potentially be associated with the loop.

The upper right panel shows the F277W−F444W color map of the same region. Although the north part of the loop seems to be associated with galaxy A, this galaxy is redder than the stream and the galaxies of the cluster. In fact, it has a photometric redshift of 1.82 (Coe et al. 2019), placing it behind the cluster and not physically associated with the stream. Galaxy B, on the other hand, has colors that are compatible with those of the stream. The photometric redshift of this galaxy is 0.32 (Coe et al. 2019). However, the position of this galaxy is inconsistent with having created the entire giant west loop. Another option is that the loop is the remnant of a galaxy that has already been stripped or has merged and is no longer identifiable.

Both east streams are shown in the lower panels of Figure 4. East stream 1 is narrower (with a width of ∼15 kpc) than the other features highlighted in this paper. In the color map (lower right panel), this feature does not show up, as there is little contrast between the stream and the ICL background (see also Figure 3). The color and width of this stream potentially associate it with galaxy C. East stream 2 is wider (∼30 kpc), likely produced by the stripping of galaxy D. This stream has a similar color to the ICL in the inner parts of the cluster, as seen in the color map.

The widths of both the giant west loop and east stream 2 are compatible with the size of Milky Way–like objects (i.e., with a diameter of ∼30–40 kpc; Trujillo et al. 2020). This is in agreement with the finding that the stars composing the ICL are mainly stripped from the outskirts of galaxies with stellar masses around $5 \times 10^{10}\ M_{\odot}$ (Montes & Trujillo 2014; Morishita et al. 2017; DeMaio et al. 2018; Montes & Trujillo 2018).

4.1.2. Plumes

The plumes seen in the center of the cluster from ∼25 to 100 kpc (Figure 1) indicate that the BCG of this cluster is likely experiencing a merger (see also Duc et al. 2015; Martin et al. 2022). At the same time, the measured color is flat in the inner

∼100 kpc in both the east and west profiles, indicating that the stellar populations in this region are well mixed. Flat gradients in color are indicative of stars expelled into the intracluster medium during a major merger (<1:10; Krick & Bernstein 2007; DeMaio et al. 2015, 2018). The major merger is likely with the galaxy located 9″ (∼47 kpc) away to its west, as both galaxies are connected by a stellar bridge (zoom-in in Figure 1). Assuming similar stellar population properties between both galaxies, the merger ratio inferred is 1:3.

The distinct features that compose the diffuse light of this cluster (plumes, streams, loop, etc.) suggest different physical mechanisms creating the ICL in this cluster (mergers and tidal disruption). This is telling us that the mechanisms that contribute to the bulk of ICL formation are different depending on their distance to the center of SMACS 0723.

4.2. The Slope of the Stellar Mass Density of the ICL

The high degree of structure in the ICL of this cluster suggests that the diffuse extended component is being built now. Thanks to the dense environment of the cluster, in a few gigayears, these structures will smooth and become well mixed (Rudick et al. 2011). Over time, the tidal stripping of more and more satellites will build the outer ICL (DeMaio et al. 2018, 2020).

To get an estimation of the slope of the stellar mass density profile, we have fitted a power law to the BCG+ICL profile shown in the right panel of Figure 3. It shows two different density profiles: $M/L = 0.7$ (solid lines; $[M/H] = 0.22$, 7 Gyr) and $M/L = 0.18$ (dashed lines; $[M/H] = -0.7$, 1.5 Gyr). We used the fact that the centers of BCGs are usually old and high in metallicity to fix the center of the profiles to the $M/L = 0.7$ value. As we expect a gradient in metallicity, and probably age, the true density profile in the outer parts will range between the $M/L = 0.7$ and 0.18 profiles. As an example, we represent this range of possible solutions with a gray shaded region in Figure 3 for the east profile, although we did that for both the east and west profiles. We fitted a power law to this range of possible solutions for both the east and west density profiles. The resulting slope and its errors encompass the possible solutions shown in Figure 3. The slope is $\alpha_{2D,E} = -1.48 \pm 0.13$ for the east profile and $\alpha_{2D,W} = -1.46 \pm 0.08$ for the west profile. Both values are in agreement within the errors. That translates into a 3D slope of ~ -2.47 (Equation (5) in Stark 1977). The value of the 3D slope is in agreement with the values of the slopes in Montes & Trujillo (2018) for the Frontier Fields clusters. This result implies that the stellar halo and the dark matter of SMACS 0723 could have similar slopes (the dark matter slopes range between −2.6 and −2; Pillepich et al. 2014, 2018), something expected for high-mass clusters ($M_h = 8.39^{+0.33}_{-0.34} \times 10^{14} M_\odot$; Coe et al. 2019).

In this work, we present the first analysis of the ICL of the ERO observations with JWST. We rereduced the original JWST released images to minimize the inhomogeneities and make them more suitable for ICL studies. After our reprocessing, we measured that the ICL covers around half of the NIRCam detector area. We derived the surface brightness radial profiles out to 380 kpc from the center of the BCG and the F277W−F444W color profiles to 300 kpc. We found the following.

1. The ICL of SMACS 0723 presents a lot of substructure indicating that the processes that form the ICL in this cluster are caught in action.
2. The color and morphological properties of the ICL in the inner ∼100 kpc are consistent with a major merger.
3. The outer ICL (>150 kpc) is being formed by the tidal stripping of Milky Way–like galaxies.
4. The slope of the stellar mass density profile of the BCG +ICL ($\alpha_{3D} = -2.47 \pm 0.13$) is nearly identical to the slope of the dark matter profile of clusters of this mass. This reinforces the idea of using the ICL as a potential dark matter tracer. Considering this, we encourage using the ICL to improve the gravitational lensing mass maps and, consequently, the characterization of the properties of the first galaxies.

We would like to thank the referee for the useful comments that improved this manuscript. This publication is part of project PCI2021-122072-2B, financed by MICIN/AEI/10.13039/501100011033, and the European Union NextGenerationEU/RTRP. I.T. acknowledges support from the ACIISI, Consejería de Economía, Conocimiento y Empleo del Gobierno de Canarias and the European Regional Development Fund (ERDF) under a grant with reference PROID2021010044 and the State Research Agency (AEI-MCINN) of the Spanish Ministry of Science and Innovation under grant PID2019-107427GB-C32 and IAC project P/300624, financed by the Ministry of Science and Innovation, through the State Budget and by the Canary Islands Department of Economy, Knowledge and Employment, through the Regional Budget of the Autonomous Community. The authors want to thank the JWST ERO team for making these extraordinary data available.

Facility: JWST (NIRCam).

Software: `astropy` (The Astropy Collaboration et al. 2018), SExtractor (Bertin & Arnouts 1996), SWarp (Bertin 2010), `photutils` v0.7.2 (Bradley et al. 2019), `pillow` (van Kemenade et al. 2020), `numpy` (Oliphant 2006), `scipy` (Virtanen et al. 2020).

Appendix A
Example of the Data Processing of the Images from the Long-wavelength Channel

In Section 2, we detailed the data rereduction that we performed in the JWST NIRCam images. For the long-wavelength channel, we fit a second-degree 2D polynomial (a plane) to the calibrated images to eliminate the gradient seen across the frame. For all of the filters, the gradients extend from the lower left to the upper right of the frames (left and middle panels in Figure 5). To estimate the strength of the gradient in the different frames, we measured the edge-to-edge difference along the direction of the gradient relative to the rms of the frame. We placed two boxes of 50 pixels × 50 pixels at a distance of ∼360 kpc from the BCG, one in the lower left and one in the upper right corner of the image, and calculated the median value in the masked frames. The median and dispersion of the gradients of the individual frames are (per band) $1.9 \pm 0.2\sigma$, $1.7 \pm 0.2\sigma$, and $2.0 \pm 0.1\sigma$ for F277W, F356W, and F444W, respectively.

The left panel in Figure 5 shows a stage 2 calibrated frame in the F277W band. The middle panel shows the plane fitted to the masked original calibrated frame. The right panel shows our final result without the gradient. The gradient in this example (2.1σ) is representative of the typical gradient in the individual frames of the F277W filter.

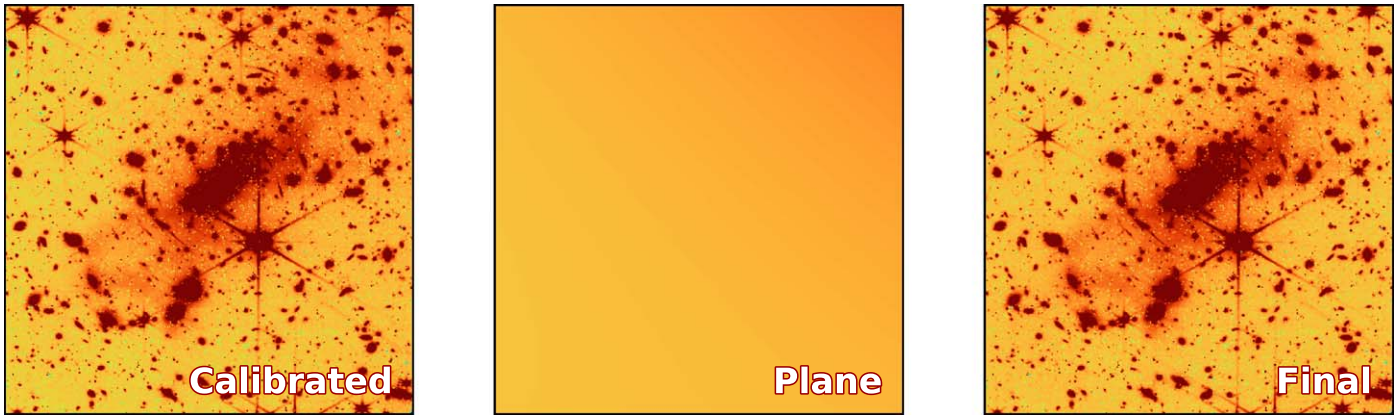

Figure 5. Example of a single frame background correction. Left panel: calibrated F277W frame (`jw02736001001_02101_00003_nrcblong_cal.fits`). A gradient across the image can be seen toward the upper right corner. Middle panel: second-degree polynomial plane fitted to the (masked) calibrated frame to correct the gradient. Right panel: final frame after subtracting the plane.

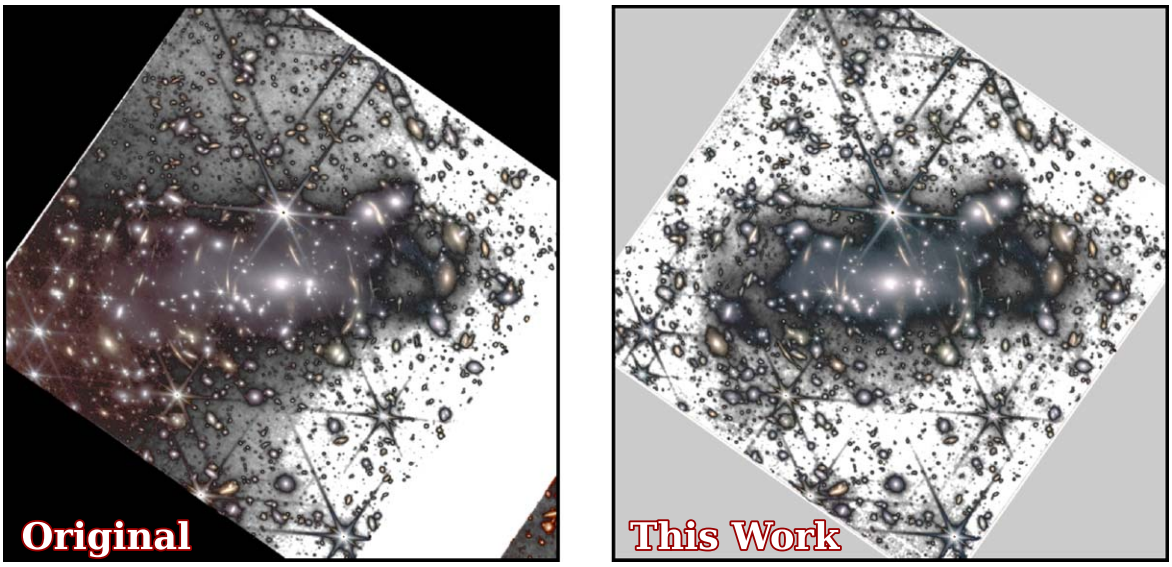

Figure 6. Left panel: RGB color-composite image using the original calibrated coadds of the long-wavelength channels. Right panel: RGB color-composite image using the rereduced coadd images created in this work. Note the huge improvement of correcting the strong light gradient toward the east side on the NIRCam.

Figure 6 shows the improvement of the final data reduction performed here. Both panels show RGB color-composite images using the long-wavelength bands and with an average of the three filters as the black-and-white background. The original images (left panel) are those using the JWST current reduction pipeline, whereas our rereduction is shown in the right panel.

To quantify the improvement of the data processing in the final coadds performed in this paper, we again measured the edge-to-edge difference along the direction of the gradients in the final coadded images relative to their rms. In this case, the gradients extend along the major axis of the cluster (i.e., east to west; Figure 6). We placed the two boxes, one to the west and one to the east, at $\sim$360 kpc from the BCG. The difference between the median values of both boxes for the original images are 3.5σ, 2.9σ, and 4.0σ for F277W, F356W, and F444W, respectively. Note the increase in the significance by a factor of around 2 of the gradient with respect to the individual frames we have discussed above. If the gradient were strictly the same in all of the individual frames that form the coadd, we should expect and increase in the signal of a factor of 3 (as we have nine individual frames per filter). We think that the lower increase in the signal reflects that the amplitude and also the direction of the individual gradients are slightly different from frame to frame. On doing the same calculation to measure the gradient in our corrected coaddition, we find that the gradients significantly decrease: 0.7σ, 0.06σ, and 0.26σ. Particularly striking is the reduction in the average of the three filters (black-and-white background in Figure 6), where the difference in the gradient is 5.3σ in the original images and 0.52σ in our reduced data set.

Appendix B
Short-wavelength Channel Rereduction

The short-wavelength channel consists of a mosaic of eight detectors (four for each module) manufactured with a 2.5 μm wavelength cutoff. In each module, the four short-wavelength detectors are arranged in a 2×2 array. The pixel scale of this channel is $0\farcs031$/pixel.

Contrary to the case of the long-wavelength channel, the detectors in the short-wavelength channel are smaller than the extent of the diffuse light of the cluster. For this reason, fitting a plane to each one of the detectors is risky, more so when the gradients in the different detectors are not consistent in direction, as was the case for the long-wavelength channel.

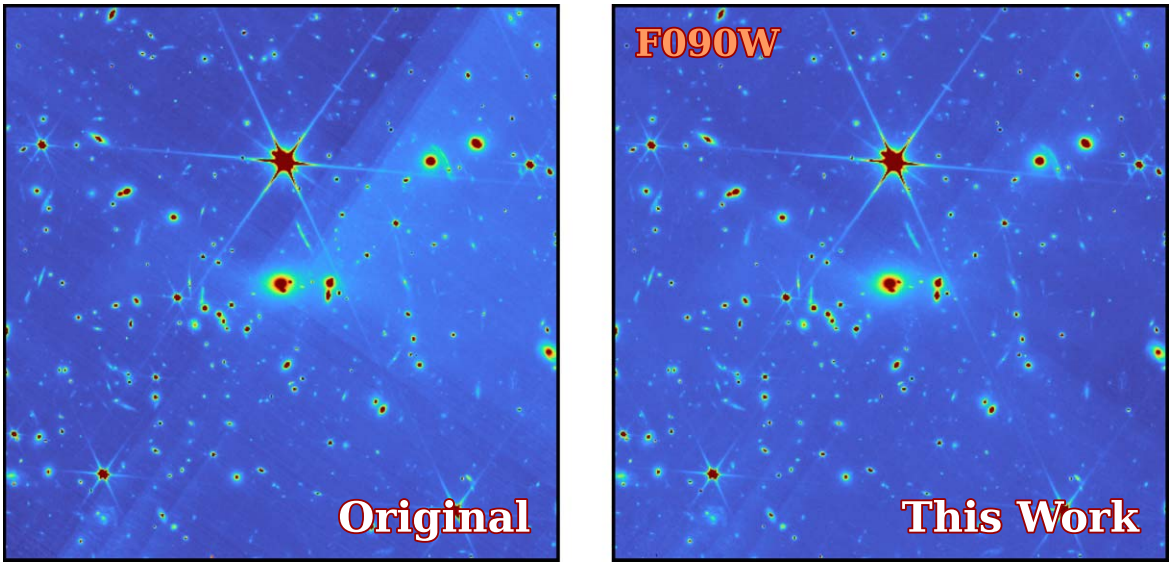

Figure 7. Left panel: original calibrated F090W coadd. Right panel: final coadd after the data rereduction.

In this case, we opted for a more conservative approach: to correct for the readout pattern per detector (see Merlin et al. 2022; Pontoppidan et al. 2022) and scale the four detectors.

One of the characteristics of the NIRCam detectors is the presence of low-level electronic noise manifesting as linear stripes ("1/f noise"; see also Pontoppidan et al. 2022). The released ERO images are already corrected from this noise using a simple correction. However, residuals are left, clearly visible in the short-wavelength channel images (left panel of Figure 7).

The first step was to remove this remaining pattern by subtracting the 3σ-clipped median value for each row, horizontally, in the calibrated individual frames after masking out all the objects. Once this correction was applied, we derived an improved mask from the corrected images and computed and repeated the process with this later mask, i.e., subtracted the median value for each row in the masked individual frames.

Once the images per detector were corrected from the remaining 1/f noise, we built the mosaics. The left panel of Figure 7 shows that in the final calibrated mosaics, the different detectors were not properly scaled. Therefore, we have also scaled the mosaics by multiplying each detector by a factor between 0.9 and 1.1, taking detector one (`nrcb1`) as reference. This factor is computed as the 3σ-clipped median for each frame in a ring of radius $\sim 47''$ and width of $6''$ from the center of the frame after masking all sources. After scaling the different detectors, the frames were assembled using `SWarp`. The final output is created as the median of the nine mosaic frames.

An example of the data reduction for the F090W band is shown in Figure 7. For comparison, we show the original image in the left panel and our data reduction in the right panel. In this case, the difference along the direction of the gradient (see Appendix A) is 2.5σ in the original image and 0.6σ in our rereduction. Despite the clear improvement, the final images of the short-wavelength channel still show significant residuals that prevent us from using them to study the ICL. These residuals seem to be caused by inhomogeneities in the four different adjacent sectors (512×2048 pixels) that form each of the detectors.[6]

[6] https://www.stsci.edu/files/live/sites/www/files/home/jwst/documentation/technical-documents/_documents/JWST-STScI-001721.pdf

Appendix C
From MJy sr^{-1} to Surface Brightness in JWST Data

In this work, all of the units of the photometry, surface brightness, and color profiles are given in mag arcsec^{-2} (in the AB system). The explicit equation to transform from MJy sr^{-1} (the units of the JWST images) to surface brightness in the AB system is

$$\mu_{\rm AB} = -2.5 \times \log_{10}\left[\left(\text{counts [MJysr}^{-1}] \times \frac{10^6}{4.25 \times 10^{10}}\right)\right] + 8.906, \quad \text{(C1)}$$

where 4.25×10^{10} corresponds to the number of square arcseconds in 1 sr. The factor 10^6 stands for the transformation from megajanskys to janskys. Finally, the 8.906 value corresponds to the AB system that referred to 3631 Jy as the reference unit (Oke & Gunn 1983).

ORCID iDs

Mireia Montes https://orcid.org/0000-0001-7847-0393
Ignacio Trujillo https://orcid.org/0000-0001-8647-2874

References

Adams, N. J., Conselice, C. J., Ferreira, L., et al. 2022, arXiv:2207.11217
Alonso Asensio, I., Dalla Vecchia, C., Bahé, Y. M., Barnes, D. J., & Kay, S. T. 2020, MNRAS, 494, 1859
Bertin, E. 2010, ascl.soft, ascl:1010.068
Bertin, E., & Arnouts, S. 1996, A&AS, 117, 393
Bradley, L., Sipocz, B., Robitaille, T., et al. 2019, astropy/photutils: v0.7.1, v0.7.1, Zenodo, doi:10.5281/zenodo.3478575
Cardelli, J. A., Clayton, G. C., & Mathis, J. S. 1989, ApJ, 345, 245
Coe, D., Salmon, B., Bradač, M., et al. 2019, ApJ, 884, 85
Contini, E. 2021, Galax, 9, 60
Deason, A. J., Oman, K. A., Fattahi, A., et al. 2021, MNRAS, 500, 4181
DeMaio, T., Gonzalez, A. H., Zabludoff, A., Zaritsky, D., & Bradač, M. 2015, MNRAS, 448, 1162
DeMaio, T., Gonzalez, A. H., Zabludoff, A., et al. 2018, MNRAS, 474, 3009
DeMaio, T., Gonzalez, A. H., Zabludoff, A., et al. 2020, MNRAS, 491, 3751
Duc, P.-A., Cuillandre, J.-C., Karabal, E., et al. 2015, MNRAS, 446, 120
Feldmeier, J. J., Mihos, J. C., Morrison, H. L., Rodney, S. A., & Harding, P. 2002, ApJ, 575, 779

Gonzalez, A. H., George, T., Connor, T., et al. 2021, MNRAS, 507, 963
Gregg, M. D., & West, M. J. 1998, Natur, 396, 549
Iodice, E., Spavone, M., Cantiello, M., et al. 2017, ApJ, 851, 75
Kluge, M., Neureiter, B., Riffeser, A., et al. 2020, ApJS, 247, 43
Krick, J. E., & Bernstein, R. A. 2007, AJ, 134, 466
Lauer, T. R. 1988, ApJ, 325, 49
Mahler, G., Jauzac, M., Richard, J., et al. 2022, arXiv:2207.07101
Martin, G., Bazkiaei, A. E., Spavone, M., et al. 2022, MNRAS, 513, 1459
Merlin, E., Bonchi, A., Paris, D., et al. 2022, ApJ, 938, L14
Mihos, J. C., Harding, P., Feldmeier, J., & Morrison, H. 2005, ApJL, 631, L41
Mihos, J. C., Harding, P., Feldmeier, J. J., et al. 2017, ApJ, 834, 16
Montes, M. 2019, arXiv:1912.01616
Montes, M. 2022, NatAs, 6, 308
Montes, M., Brough, S., Owers, M. S., & Santucci, G. 2021, ApJ, 910, 45
Montes, M., & Trujillo, I. 2014, ApJ, 794, 137
Montes, M., & Trujillo, I. 2018, MNRAS, 474, 917
Montes, M., & Trujillo, I. 2019, MNRAS, 482, 2838
Morishita, T., Abramson, L. E., Treu, T., et al. 2017, ApJ, 846, 139
Oke, J. B., & Gunn, J. E. 1983, ApJ, 266, 713
Oliphant, T. E. 2006, A Guide to NumPy, Vol. 1 (USA: Trelgol Publishing)
Pillepich, A., Nelson, D., Hernquist, L., et al. 2018, MNRAS, 475, 648
Pillepich, A., Vogelsberger, M., Deason, A., et al. 2014, MNRAS, 444, 237
Pontoppidan, K., Blome, C., Braun, H., et al. 2022, ApJL, 936, 14
Repp, A., & Ebeling, H. 2018, MNRAS, 479, 844
Rieke, M. J., Kelly, D. M., & Horner, S. D. 2005, Proc. SPIE, 5904, 1
Rigby, J., Perrin, M., McElwain, M., et al. 2022, arXiv:2207.05632
Román, J., Trujillo, I., & Montes, M. 2020, A&A, 644, A42
Rudick, C. S., Mihos, J. C., & McBride, C. K. 2011, ApJ, 732, 48
Schlafly, E. F., & Finkbeiner, D. P. 2011, ApJ, 737, 103
Sheth, K., Regan, M., Hinz, J. L., et al. 2010, PASP, 122, 1397
Stark, A. A. 1977, ApJ, 213, 368
The Astropy Collaboration, Price-Whelan, A. M., Sipőcz, B. M., et al. 2018, AJ, 156, 123
Trujillo, I., Chamba, N., & Knapen, J. H. 2020, MNRAS, 493, 87
van Kemenade, H., wiredfool, Murray, A., et al. 2020, python-pillow/Pillow 7.1.1, Zenodo, doi:10.5281/zenodo.3738618
Vazdekis, A., Koleva, M., Ricciardelli, E., Röck, B., & Falcón-Barroso, J. 2016, MNRAS, 463, 3409
Virtanen, P., Gommers, R., Oliphant, T. E., et al. 2020, Nat. Methods, 17, 261
White, S. D. M. 1980, MNRAS, 191, 1P
Worthey, G. 1994, ApJS, 95, 107